

Contents lists available at ScienceDirect

Acta Materialia

journal homepage: www.elsevier.com/locate/actamat



Full length article

Size effects in the martensitic transformation hysteresis in Ni–Mn–Sn Heusler alloy films



Yijia Zhang ^a, Julia Billman ^b, Patrick J. Shamberger ^{a,*}

- ^a Department of Materials Science and Engineering, Texas A&M University, College Station, TX, 77843, USA
- ^b Department of Mechanical Engineering, Texas A&M University, College Station, TX, 77843, USA

ARTICLE INFO

Article history:
Received 27 May 2019
Received in revised form
28 August 2019
Accepted 3 September 2019
Available online 5 September 2019

Keywords:
Size effects
Thermal hysteresis
Martensitic phase transformation
Heusler alloy

ABSTRACT

Understanding the effect of small characteristic length scales on phase transformations requires microscopic observations to identify mechanisms which may influence the progression of the transformation. Here, we report thickness-dependent hysteresis in electrochemically deposited Ni–Mn–Sn Heusler alloy films, as observed by optical microscopy. This approach allows for analyzing size dependent phase transformation behavior within individual grains from films with decreasing thickness. Hysteresis is not correlated with grain size, but increases with decreasing film thickness following a power law relationship. This behavior is attributable to internal friction-induced energy dissipation at the film/ substrate interface in microscale alloy films.

© 2019 Acta Materialia Inc. Published by Elsevier Ltd. All rights reserved.

1. Introduction

Martensitic phase transformations are responsible for multifunctional behavior due to changes in shape, magnetization, and enthalpy associated with the phase transition [1–4]. Over the past decade, the primary thrust of magnetocaloric material research has been focused on coupling large caloric effects with low hysteresis for maximizing the efficiency of a cooling or heat pump cycle [5–13]. Simultaneously, size effects are becoming increasingly important as the critical length scale of different morphologies of caloric effect materials (wires, micro-spheres, films, etc.) are being decreased in order to enhance heat transfer from the caloric effect material into a heat transfer fluid [14-16]. Decreasing the characteristic length scales of multifunctional alloys, including sample grain size or sample dimensions, could impact the behavior of solid-state martensitic phase transformations and hysteresis by introducing additional surfaces and interfaces. These additional surfaces and interfaces modify the surface to volumetric free energy terms, and also interact with and potentially impede mobile interphase boundaries. In order to develop micro- and nanoscale multifunctional devices, a mechanistic understanding of the role of size effects on phase transformations in multifunctional alloys at small length scales is required [17–21]. In particular, it is critical to distinguish between effects associated with grain size and sample dimensions in order to decrease the hysteresis loss and improve the durability of small-scale multifunctional alloys.

Hysteresis, which generally occurs in any process which must overcome an energy barrier separating an initial state from a relaxed equilibrium state, results in a deviation from equilibrium and consequentially, entropy generation [22]. Small critical length scales in a material impact hysteresis by several different previously observed mechanisms, including 1) the reliance of nucleation on relatively sparse high-energy nucleation sites, 2) the introduction of additional frictional work associated with the forward or reverse phase transformations, or 3) the rate of conductive heat transfer with a non-negligible critical time associated with sample dimensions [22-25]. Decreased sample volume could decrease the probability of heterogeneous nucleation within a given particle due to the low probability of including relatively sparse high-energy active nucleation sites within a given volume [24-26]. Internal frictional work, which is dissipated due to the presence of frictional barriers opposing the motion of the martensite-austenite interfaces, generally increases with an increase in the density of grain boundary interfaces or free surfaces [22,23]. Finally, large samples could show rate-dependent hysteresis due simply to significant thermal heterogeneities, which result from the finite time required for a volume to thermally homogenize [23]. While each of these mechanisms have been observed in different systems, what

^{*} Corresponding author. E-mail address: patrick.shamberger@tamu.edu (P.J. Shamberger).

remains relatively unclear are the relative magnitudes associated with different mechanisms across the characteristic length scales of a material, most notably with grain size and with sample dimensions. This distinction has been difficult to resolve due to correlations between the two variables, as well as a strong reliance on macroscopic observables, (e.g., strain, magnetization, enthalpy), rather than microscopic observations.

Grain size has been observed to impact phase transformation critical temperatures and stresses, as well as transformation hysteresis [27–34]. In particular, martensite start temperatures (M_s) decreased with decreasing grain size in bulk polycrystalline alloys when grain size was smaller than 130 µm [27–33]. This phenomenon was explained by the Hall-Petch relationship based on enhanced barrier effects of grain boundaries due to dislocation pileups in small grains [28,31]. In millimeter-scale wires or sheets, where grain size decreases but the critical sample dimensions are also small, a relative grain size parameter, the ratio of grain size to sample dimension, has been introduced [34-39]. It was found that the martensite start stresses increased with the decreasing of the ratios [36-39]. Although these works report the impact of grain size on phase transformation temperatures and stresses, grain size also impacts transformation hysteresis. With decreasing grain size in Cu-Al-Be bars and the decreasing of the ratio of grain size to sample dimension in Cu-Al-Mn-based wires, the stress hysteresis increased [34,35]. These increased martensite start stresses and stress hysteresis at smaller size ratios were caused by the increased degree of grain constraint, associated with increased barrier heights for the transformations to occur based on the Hall-Petch relationship discussed previously [34–38]. A similar constraint came from nanoscale grains due to a high grain boundary density has been presented in nanocrystalline NiTi alloys [40-43]. With the decreasing of grain size, the increased density of grain boundaries acted as obstacles and impeded the propagation of austenite/ martensite interfaces through a volume [40,41].

The effects of sample dimensions on martensitic phase transformation behavior have been investigated in several shapes, including thin films, micro/nanopillars, and microwires [14,17,23,44–51]. These materials with different shapes could be categorized into two groups, one group has confinement from elastically clamped boundaries (e.g., thin films on substrates), while the other group has free boundaries (e.g., micro/nanopillars). Correspondingly, the interactions between sample dimension and transformation behavior are more complicated than the effect of grain size based on the Hall-Petch relationship. With decreasing film thickness, epitaxial thin films (10-200 nm) without grain boundaries showed broader transformation ranges and decreased phase transformation temperatures, which were explained by possible residual austenite layers and increased lattice mismatch at the film/substrate interface [14]. When the film thickness was smaller than 40 nm, the martensite transformation was inhibited by the increased lattice mismatch at the film/substrate interface [32]. For thicker films ($<1 \mu m$), thickness effects based on residual tensile stress in films resulting from growth of these films can also exhibit additional complications from surface oxide layers, which introduced a compositional gradient [44,50,51]. With decreasing film thickness (<100 nm), the residual tensile stress generally overwhelmed other contributions, resulting in an increase in both the austenite finish temperatures (A_f) and M_s [44].

In contrast, micro/nanopillars with unconstrained structures are suitable to study intrinsic size effects on superelasticity in the absence of elastic confinement/substrate effects [17,47–49]. With decreasing pillar diameter, the stress hysteresis either decreased or increased in different systems due to the interaction between two

competing phenomena: 1) the strengthening of crystals due to dislocation starvation, which has been observed in Ni-based pillars [48], and 2) decreased probability of heterogeneous nucleation due to the lack of high-energy nucleation sites [47]. Microwires with a free boundary showed increased thermal and stress hysteresis with the decreasing of wire diameters, which were attributed to the internal friction-induced energy dissipation at the free surface with defects by analyzing Gibbs free energy density change [23].

Here, we report thickness-dependent hysteresis in electrochemically deposited microscale Ni-Mn-Sn Heusler alloy films by statistical analysis of phase transformation behavior in individual grains. Electrochemical deposition is used because it is able to deposit either thick or thin films with low surface roughness and controllable composition and microstructure [52-54].Ni_{0.48}Mn_{0.40}Sn_{0.12} Heusler alloy films with decreasing thickness, 14.5, 8.7, and 2.9 µm, are synthesized by annealing electrochemically deposited multi-layer monatomic (Ni, Mn, Sn) films following a technique described in more detail elsewhere [54]. Phase transformation temperatures and sizes of nearly four hundred grains on each film are collected optically while the samples are heated or cooled. While hysteresis is not correlated with grain size within a given film, it is dependent on film thickness following a power law relationship. Nucleation-limited transfer motion behavior is not observed in these films. Rather, we infer that the thickness effects in thermal hysteresis in microscale alloy films are attributable to internal friction-induced energy dissipation at the film/substrate interface.

2. Experimental

 $Ni_{0.48}Mn_{0.40}Sn_{0.12}$ alloy films of thickness, 14.5, 8.7, and 2.9 μ m, were synthesized by post-annealed multi-layer films using electrochemical deposition in multi-pot aqueous solutions. Details of our processing route were described elsewhere [54]. Briefly, fifteen-layer (W//[Mn/Ni/Sn]₅, 14.5 μm), nine-layer (W//[Mn/Ni/ Sn_{3} , 8.7 μ m), and triple-layer (W//[Mn/Ni/Sn], 2.9 μ m) films were deposited on tungsten substrates by repeated stacking of monatomic Mn, Ni, and Sn films. Homogeneous single-phase Ni_{0.48}Mn_{0.40}Sn_{0.12} alloy films were obtained by annealing the multi-layer films. Films were heated to 210 °C (30 °C/min) and annealed for 20 min, heated to 900 °C (30 °C/min) and annealed for 20 min, then finally heated to 1000 °C (10 °C/min) and annealed for 1 min. This sequence promoted chemical homogenization, while mitigating the tendency for low melting point monatomic layers to melt. A schematic diagram of the cross-section of a homogeneous Ni-Mn-Sn alloy film, which comes from electrochemically deposited nine-layer (W//[Mn/Ni/Sn]₃, 28.9 µm) films, illustrates successful deposition of stacked monatomic layers resulting in a homogeneous single-phase alloy after annealing (Fig. 1). Film compositions were verified by energy dispersive spectroscopy (EDS) (Fig. S1). Phases and crystal structures of alloy films at 45 °C (martensite with 14M monoclinic structure) and 115 °C (austenite with L2₁ cubic structure) were identified by X-ray diffraction (XRD) (Fig. 2) [55,56]. The crystal structures of martensite and austenite phases in alloy films with different thicknesses were the same. A cross-section image of the 14.5 µm thick alloy film showed uniform film thickness (Fig. S2).

Electrochemical deposition of multi-layer films was performed with a Biologic SP-150 potentiostat using a standard three-electrode configuration. Details about deposition solution, electrodes, and current densities were described elsewhere [54]. A tube furnace was used for annealing multi-layer films with argon (purity 99.999%)-5% hydrogen forming gas at 101 kPa. An in-line desiccant

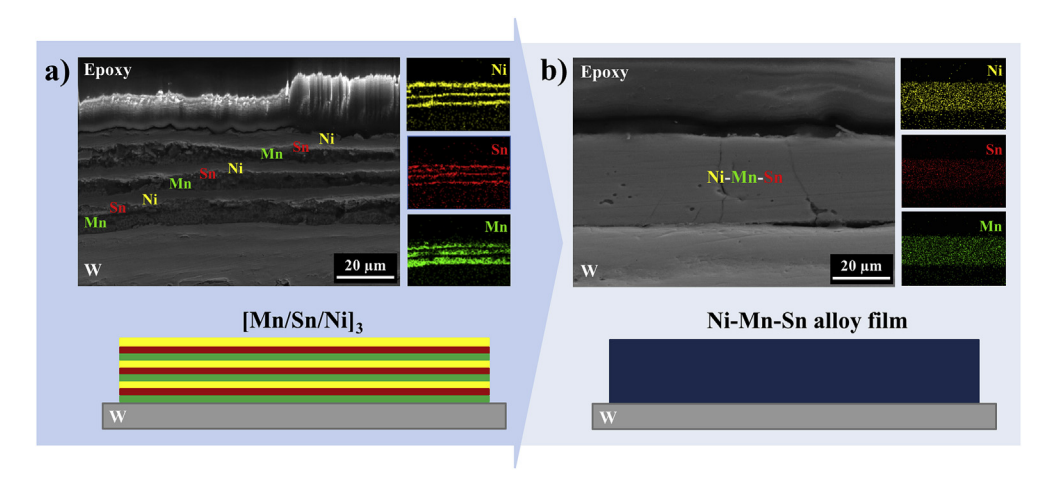


Fig. 1. a) Cross-section of electrochemically deposited nine-layer (W//[Mn/Ni/Sn]₃) films on tungsten substrates (left), including Ni (yellow), Sn (red), and Mn (green) element mapping by EDS [54]. b) Cross-section of the same film after the annealing sequence described in the text, suggesting a homogeneous single-phase alloy. (For interpretation of the references to colour in this figure legend, the reader is referred to the Web version of this article.)

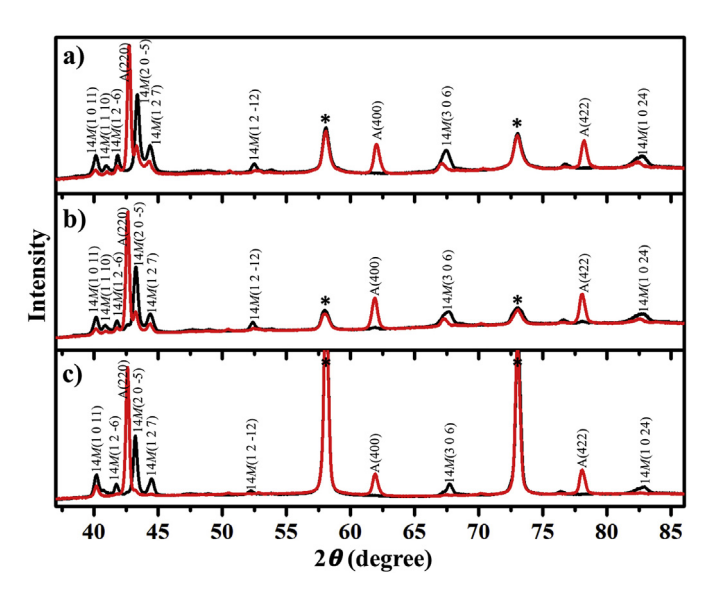


Fig. 2. XRD patterns of a) 14.5 μ m thick, b) 8.7 μ m thick, and c) 2.9 μ m thick alloy films at 45 °C (black) and 115 °C (red) [55,56]. Cubic W substrate reflections were marked with asterisks. (For interpretation of the references to colour in this figure legend, the reader is referred to the Web version of this article.)

and oxygen getter (Restek), titanium sponges (Alfa Aesar), and titanium envelopes (Alfa Aesar) were used to trap oxygen and water and purify forming gas.

SEM was carried out on Tescan Lyra-3 equipped with an Oxford EDS at 20 keV accelerating voltage (secondary electron imaging mode). XRD measurements were performed by a Bruker D8 Discover with an area detector (VÅNTEC 500), with Cu K α radiation equipped with a custom peltier temperature controlled stage $(45-115)\pm0.1\,^{\circ}\text{C}$. A TA Instrument (Q2000 DSC) was used for DSC tests with $10\,^{\circ}\text{C/min}$ heating and cooling rates under a nitrogen atmosphere. Optical observation of phase transformation was performed on a BX53M Olympus upright microscope equipped with a differential interference contrast (DIC) prism and a Linkam LTS 120 temperature controlled microscope stage (-25 to $120)\pm0.1\,^{\circ}\text{C}$. JMP Pro 13 software was used to classify grain phase transformation data for probability histograms and outlier box plots. ImageJ software was used to obtain grain area.

3. Results

3.1. Phase transformation progression within a grain

Phase transformations were analyzed within individual grains in order to correlate the nucleation and growth of martensitic domains with the overall extent of phase transformation. Three grains were selected randomly from each thickness films (14.5, 8.7, and 2.9 μm thick; Table 1) and the area fraction of each grain containing martensite during heating and cooling was calculated using standard image analysis techniques (Fig. 3a,b,c). The A_f (or M_s) temperature of a grain was defined as the temperature at the last (or first) observed surface deformation on heating (or cooling) associated with twinning in the martensite phase. During both heating and cooling transformations, contraction or growth of martensite domains in each grain initiated slowly, followed by a rapid change in martensite content which tapers off dramatically as the transformation concludes. In all cases, complete transformation occurred over a span of more than 10 °C for both heating and cooling transformations. Grains 2 and 8 were used as examples of large and small grains, respectively, to show the contraction and growth of martensite domains during grain phase transformation (Fig. 3d and e). In grain 2, martensite domains shrank slowly from 97 to 100 °C, shrank rapidly from 100 to 102 °C, and shrank slowly from 102 to 109 °C during cooling (Fig. 3d). Martensite domains formed slowly from 105 to 98 °C, formed rapidly from 98 to 96 °C, and formed slowly from 96 to 93 °C during heating. During the rapid formation of martensite domains, some martensite plates (at 98 °C) dramatically grew in size (yellow dashed line), while other regions composed of multiple martensite plates abruptly appeared on the surface (green and red dashed lines). This could suggest either growth of underlying plates to intersect the surface, or abrupt auto nucleation and growth in this region. This phenomenon was also observed in grain 8 (Fig. 3e). This progression is consistent with previous observations of thermoelastic martensitic transformation, where continuous nucleation and growth of martensite domains occurs throughout the region of phase coexistence to maintain local thermal and elastic equilibria in the system [22,57].

To improve the counting statistics of phase transformations within individual grains, the thermal hysteresis ($\Delta T_0^{hyst} = A_{\rm f} - M_{\rm s}$) is adopted in this study as an accessible measure of hysteresis. Thus, it is important to demonstrate convergence between ΔT_0^{hyst} and other

Table 1 Area, phase transformation temperatures, and hysteresis in select grains.

Grain	1	2	3	4	5	6	7	8	9
Grain area, S (μm²)	1551	2599	2178	201	462	701	87	125	181
Film thickness, t (μ m)	14.5	14.5	14.5	8.7	8.7	8.7	2.9	2.9	2.9
\overline{D}^{a}/t	3.1	4.0	3.6	1.8	2.8	3.4	3.6	4.4	5.2
$A_{\rm f}$ (°C)	92	109	110	105	106	107	94	114	117
$M_{\rm s}$ (°C)	85	105	106	94	96	99	78	101	107
ΔT_0^{hyst} (°C) ^b	7	4	4	11	10	8	16	13	10
ΔT_{50}^{hyst} (°C) ^c	5.6	3.5	3.6	10.9	8.5	8.0	16.1	11.9	10.5
$E_{\rm diss}$ (J/mol ^d)	17.3	11.1	10.2	32.8	24.9	22.7	45.9	34.7	31.1

d Per mole of atoms.

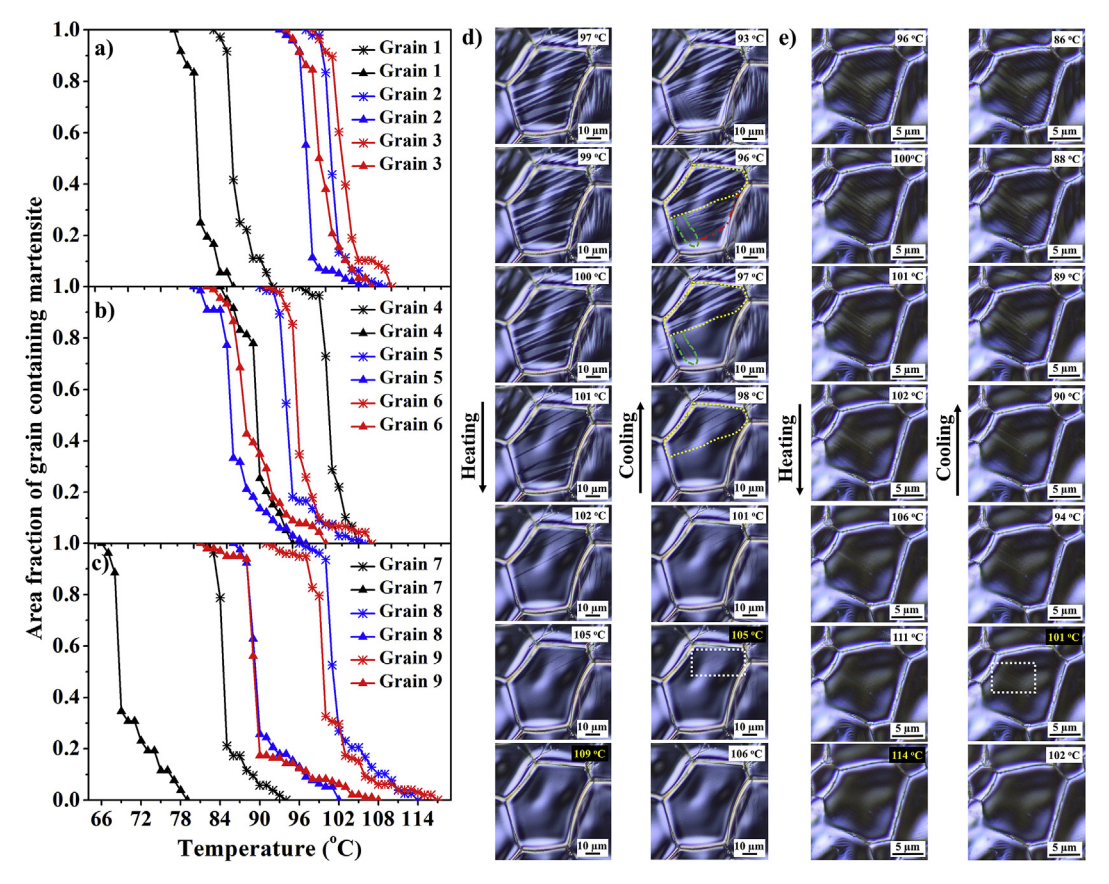


Fig. 3. The area fraction of the grain containing martensite, φ, during heating (line with asterisk) and cooling (line with triangle) in a) 14.5 μm thick, b) 8.7 μm thick, and c) 2.9 μm thick alloy films. Phase transformation processes of d) grain 2 and e) grain 8 observed by DIC.

measures of hysteresis, including $\varDelta T_{50}^{hyst}=A_{50}-M_{50}$, as well as the energy dissipated each cycle ($E_{\rm diss}$) during the phase transformations. Under the assumptions that 1) frictional work is the only source of irreversible dissipation, 2) the internal energy change and the entropy change of the universe (surrounding plus specimens) equal to zero, and 3) the heat capacity of martensite equals to the heat capacity of austenite, the energy dissipated each cycle, E_{diss} , is given by [22].

$$E_{\text{diss}} = \frac{Q_{\text{M}}}{T_{\text{M}}} (T_{\text{A}} - T_{\text{M}}) = \Delta S_{\text{M}} (T_{\text{A}} - T_{\text{M}})$$
 (1)

where ΔS_M is the entropy change, Q_M is the absolute value of the heat evolved, and $T_{\rm M}$ and $T_{\rm A}$ are the temperatures during the cooling (M) and heating (A) transformations. According to Equation (1), when we use the entropy change and temperature as coordinates, E_{diss} of grains is represented by the area inside the cycle. Taking into account the finite transformation width observed on both the heating (martensite to austenite) and cooling (austenite to martensite) transformations, E_{diss} can be generalized as [22].

$$E_{\rm diss} = \Delta S_{\rm M} \oint \phi dT \tag{2}$$

where ϕ represents the fraction of martensite present around a complete cycle. The entropy change (ΔS_{NiMnSn}) Ni_{0.48}Mn_{0.40}Sn_{0.12} alloys with nearly 8.1 valence electron concentration (e/a) is 3.0 ± 0.3 J/(mol $^{\circ}$ C) [55,58]. Calculated E_{diss} using

 $[\]overline{D} = \sqrt{4S/\pi}$. $D = \sqrt{4S/\pi}$. $D = \sqrt{4S/\pi}$. $D = \sqrt{4S/\pi}$.

 $dT_{50}^{hyst} = A_{50} - M_{50}$, A_{50} or M_{50} is defined as the temperature at 50% area of grain containing martensite during heating or cooling, respectively.

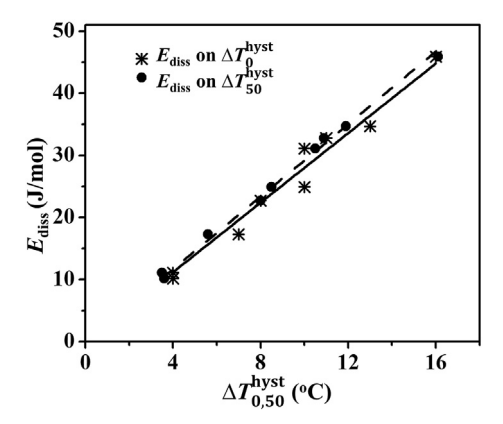


Fig. 4. Linear fits of $E_{\rm diss}$ on ΔT_0^{hyst} (solid line) or ΔT_{50}^{hyst} (dashed line) of grains in Fig. 3a,b,c.

Equation (2) and this entropy change are reported in Table 1. The linear fits of calculated $E_{\rm diss}$ on ΔT_0^{hyst} ($E_{\rm diss}=(2.80\pm0.07)$ ΔT_0^{hyst} , coefficient of determination $R^2=0.99$) or on ΔT_{50}^{hyst} ($E_{\rm diss}=(2.91\pm0.03)$ ΔT_{50}^{hyst} , $R^2=0.99$) are shown in Fig. 4. The linear models fit with $R^2\approx 1$, which demonstrate that $\Delta T_{0,50}^{hyst}$ is linearly proportional to $E_{\rm diss}$, which is calculated by the more complete mapping determined by the area fraction transformed as a function of temperature. Thus, the thermal hysteresis, ΔT_0^{hyst} or ΔT_{50}^{hyst} , is a robust measure of the energy dissipated each cycle during the phase transformations.

3.2. Thickness-dependent hysteresis

Phase transformation behavior of grains in alloy films ($Ni_{0.48}Mn_{0.40}Sn_{0.12}$) with decreasing thickness, 14.5, 8.7, and 2.9 μ m, was optically observed using DIC, while the samples were heated or cooled at 1 °C/min. This process was illustrated in one grain in a 14.5 μ m thick alloy film as an example. 108 °C was recorded as $A_{\rm f}$ temperature when the last twin disappeared completely on this grain and 105 °C was recorded as $M_{\rm s}$ temperature when the first twin formed abruptly on this grain (Fig. 5). More detailed images containing the entirety of the phase transformation process of this grain are shown in Fig. S3.

Statistical analysis of $A_{\rm f}$ and $M_{\rm s}$ temperatures, which were collected for nearly four hundred grains in each film thickness, shows thickness-dependent hysteresis. $A_{\rm f}$ and $M_{\rm s}$ temperatures of 382, 428, and 470 individual grains (in 14.5, 8.7, and 2.9 µm thick alloy films, respectively) were collected and binned in four degree increments during heating and cooling (Fig. 6a,b,c). For the 14.5 µm thick alloy film, the distributions of both collected $A_{\rm f}$ and $M_{\rm s}$ temperatures are unimodal. They are left-skewed with skewness coefficient -1.0 and -0.9 and the outlier box plots indicate numerous outliers. For 8.7 and 2.9 µm thick alloy films, the distributions of both collected $A_{\rm f}$ and $M_{\rm s}$ temperatures are also unimodal. They are left-skewed with skewness coefficient -0.7 ($A_{\rm f}$, 8.7 µm), -0.6 ($M_{\rm s}$, 8.7 µm), -0.6 ($M_{\rm f}$, 2.9 µm), and -0.5 ($M_{\rm s}$, 2.9 µm). Here, median $A_{\rm f}$ and $M_{\rm s}$ temperatures are used as they are less sensitive to skewness and outliers in the data (Fig. 6a,b,c).

Representative hysteresis for each film $(\varDelta T_0^{hyst} = A_f - M_s)$ increases with decreasing film thickness. Using the median A_f and M_s temperatures for each film, $\varDelta T_0^{hyst}$ of 14.5, 8.7, and 2.9 µm thick alloy films are 4.9, 9.7, and 15.7 °C, respectively. DSC was used to measure film hysteresis width, $\varDelta T_{DSC}^{hyst}$, which was calculated by subtracting exothermic peak temperature from endothermic peak temperature. $\varDelta T_{DSC}^{hyst}$ of 14.5 and 8.7 µm thick alloy films are 5.0 (101.3 – 96.3) and 9.1 (99.9 – 90.8) °C, respectively (Fig. S4). For the 2.9 µm thick alloy film, it is difficult to identify the endothermic and exothermic peak temperatures from DSC curves. $\varDelta T_0^{hyst}$, which is proportional to energy dissipation during transformation, is close to $\varDelta T_{DSC}^{hyst}$ for 14.5 and 8.7 µm thick alloy films. Thus, the collective thickness-dependent hysteresis of the entire film determined by DSC is in good agreement with the hysteresis determined from population statistics of individual grains. Besides, XRD measurements of each alloy film between 60 °C and 115 °C at each 5 °C during heating and cooling were performed for observing macroscopic martensitic phase transformation processes (Fig. S5). The fraction of martensite during heating and cooling, ϕ_{XRD} , is calculated by (Fig. 6d,e,f):

$$\phi_{\text{XRD}} = \frac{\widehat{I}_{\text{M}}}{\widehat{I}_{\text{M}} + \widehat{I}_{\text{A}}} \tag{3}$$

where $\hat{I}_{\rm M}$ represents the normalized combined intensity of martensite peaks (14M(1011), 14M(1110), 14M(12-6), 14M(20-5), and 14M(127)), and $\hat{I}_{\rm A}$ represents the normalized intensity of the

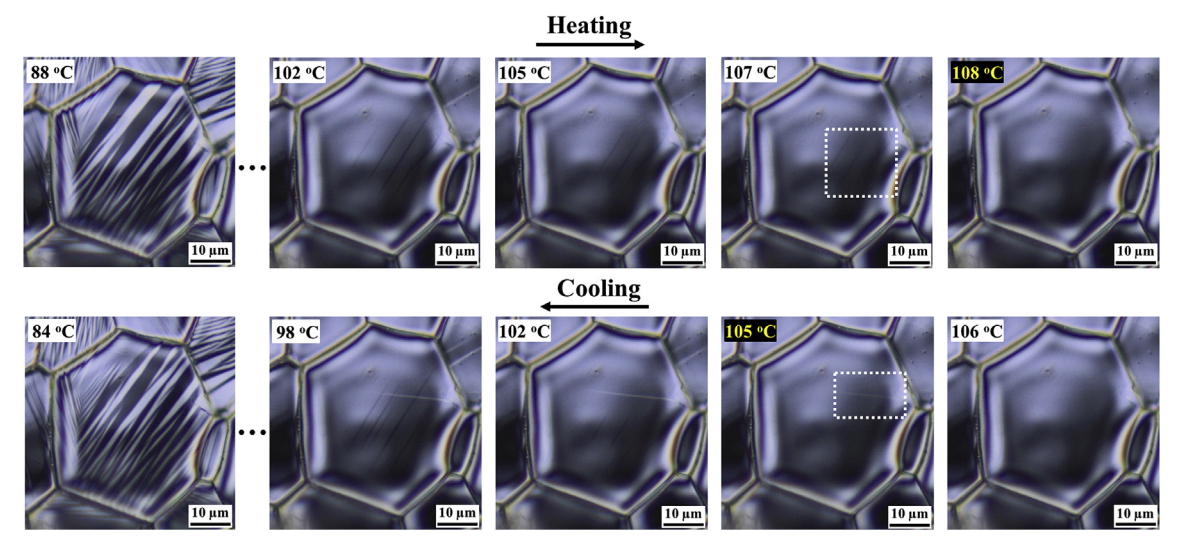


Fig. 5. Formation and disappearance of martensite domains (observed by DIC) in one grain in 14.5 μm thick alloy film during heating and cooling. 108 °C was recognized as $A_{\rm f}$ temperature and 105 °C was recognized as $M_{\rm S}$ temperature.

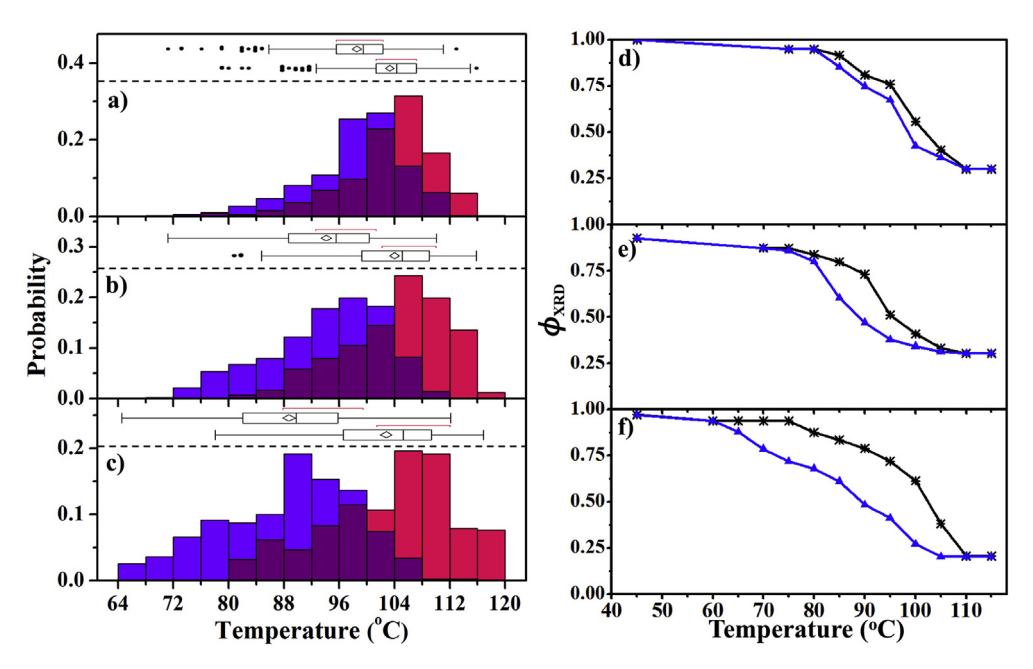


Fig. 6. Overlapping probability histograms calculated for M_s (blue) and A_f (red) for a) 14.5 μm thick, b) 8.7 μm thick, and c) 2.9 μm thick alloy films and the fraction of martensite of d) 14.5 μm thick, e) 8.7 μm thick, and f) 2.9 μm thick alloy films during heating (black line with asterisk) and cooling (blue line with triangle). Box plots for M_s and A_f are included for each alloy film. In each outlier box plot, the middle vertical line and diamond show the median and mean, respectively, while the box spans the 1st to the 3rd quartile. Points are potential outliers (disconnected points). The red brackets define the shortest half of the data (the densest region). (For interpretation of the references to colour in this figure legend, the reader is referred to the Web version of this article.)

austenite peak A(220) (Fig. S5) [55,56]. Peak intensity is measured by fitting each peak with a Gaussian peak, which resulted in excellent agreement with observed data. $\hat{I}_{\rm M}$ and $\hat{I}_{\rm A}$ are normalized by the total integral area of the measured martensite peaks at 45 °C and by the integral area of the single austenite peak at 115 °C, respectively. Alloy films have residual martensite at 115 °C, which is potentially caused by residual stress at the substrate interface, but also may reflect the limited maximum temperature available in the temperature-XRD experiment. In relation to microscopic transformation data, XRD results indicate both: 1) $E_{\rm diss}$ associated with the transformation hysteresis increases with decreasing film thicknesses (Fig. 6d,e,f), and 2) the macroscopic martensitic phase transformation in each thickness film occurs over very similar temperature ranges as that observed in the microscopic population statistics of individual grains.

 $A_{\rm f}$ and $M_{\rm s}$ temperatures of nearly four hundred grains in each film thickness show linear correlations, while ΔT_0^{hyst} just shows negligible correlations with A_f and low correlations with M_s temperatures. The A_f temperatures of the analyzed grains were plotted against their respective M_s temperatures (Fig. 7). The distribution ranges of A_f or M_S temperatures are less than 48 °C, which are likely caused by small composition or stress gradients between grains. Linear fits of A_f on M_s temperatures of grains from 14.5, 8.7, and 2.9 μ m thick alloy films with fixed slope 1 are $A_f = (4.84 \pm 0.10) + M_s$ $(R^2 = 0.89, Pearson's correlation coefficient <math>r = 0.94, A_f =$ $(10.00 \pm 0.13) + M_s(R^2 = 0.86, r = 0.93)$, and $A_f = (14.22 \pm 0.15) + M_s$ $(R^2 = 0.88, r = 0.94)$, respectively, which correspond well with ΔT_{0}^{hyst} , calculated from medians of overall populations within each film (4.9, 9.7, 15.7 °C). ΔT_0^{hyst} of collected grains is plotted against $A_{\rm f}$ or $M_{\rm S}$ temperatures and shows the random distribution of grain ΔT_0^{hyst} (Fig. S6). The correlations between grain ΔT_0^{hyst} and $A_{\rm f}$ or $M_{\rm S}$ temperatures in each film are illustrated by Pearson's correlation coefficient (r) (Table 2), when we assume that all variables are normally distributed based on diagnostic plots of their normal probabilities (Fig. S7) [59]. We only consider the absolute value of r. According to the interpretation of the size of correlation

coefficients, grain ΔT_0^{hyst} is almost independent of A_f temperatures and shows low correlations with M_S temperatures in each film [59].

4. Discussion

4.1. Mechanisms of size effects

Size effects in hysteresis of multifunctional alloys are potentially attributable to multiple mechanisms, including 1) interfacial energy, 2) surface energy, 3) acoustic emission, 4) stored elastic energy, 5) heat transfer, and 6) internal friction-induced energy dissipation during transformation [22,23,60-64]. Interfacial energy and surface energy will increase transformation stresses associated with motion of phase boundaries between martensite and austenite. Both interfacial energy and surface energy effects are generally too small to significantly impact hysteresis in microscale alloy film systems during phase transformation. For the Ni-Mn-Sn alloy film, the interfacial energy is around 0.08-0.80 J/mol, when we take the interfacial energy per unit area $\gamma_i = 1 \text{ J/m}^2$, and the interfacial area density $A_i = 10^4 - 10^5 \text{ m}^{-1}$ [60,61]. The surface energy is around 0.56 J/mol for the Ni-Mn-Sn alloy film with thickness $t = 14.5 \,\mu\text{m}$, when we take the difference in surface energy per unit area of martensite and austenite $\Delta \gamma_{sf} = 1 \text{ J/m}^2$, and the specific sample surface area $A_{sf} = 1/t$ [64]. Compared with the energy dissipated each cycle, E_{diss} (Table 1), both the interfacial energy and surface energy are negligible [55].

Acoustic emission, which is a kind of elastic wave in the ultrasonic range and is generated during the motion of interfaces between martensite and austenite, is very small and negligible in small-scale multifunctional alloys [23,65,66]. Stored elastic energy, which is related with the change in shape and volume upon the formation of martensite and elastic mismatch stresses, affects transformation stresses. This mechanism is ruled out in the Ni–Mn–Sn alloy films because that stored elastic energy is recoverable after forward transformation and does not contribute to hysteresis [23].

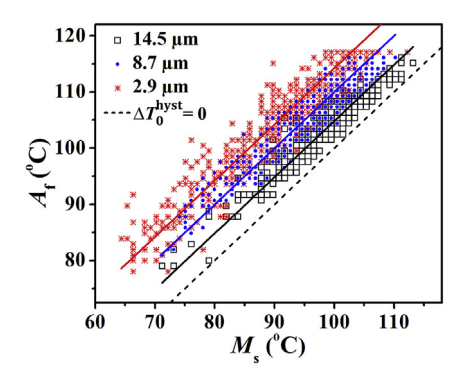


Fig. 7. Linear fits of the A_f on M_s temperatures of collected grains from 14.5 (black solid line), 8.7 (blue solid line), and 2.9 (red solid line) μ m thick alloy films. (For interpretation of the references to colour in this figure legend, the reader is referred to the Web version of this article.)

Table 2 r between grain ΔT_{Ω}^{hyst} and $A_{\rm f}$ or $M_{\rm s}$ temperatures in each film.

r	ΔT_0^{hyst} and $A_{ m f}$	ΔT_0^{hyst} and M_s
14.5 μm film	0.19	0.47
8.7 μm film	0.17	0.49
2.9 µm film	0.02	0.31

Slow rates of heat transfer in a system that is undergoing a process associated with a discontinuous enthalpy (e.g., release of latent heat) can limit the rate of that process due to development of non-uniform temperature distributions within that system. When the transformation is observed using a dynamic observation, this can result in perceived hysteresis. Sluggish heat transfer is unlikely to contribute to observed hysteresis in our microscale alloy films because of high thermal Fourier numbers (Fo) which characterize transient heat conduction in this system. A characteristic time, τ^\prime , is defined using the following equation,

$$\tau' = \frac{L^2}{\alpha} = \frac{\rho C_p L^2}{\kappa},\tag{4}$$

from which a Fo may be calculated.

$$Fo = \frac{t_{\exp}\alpha}{L^2} = \frac{t_{\exp}}{\tau'},\tag{5}$$

where L is the length through which conduction occurs, α is thermal diffusivity, C_p is specific heat capacity, is density, α is thermal conductivity, and $t_{\rm exp}$ is the experimental equilibration time (60 s) for each temperature step before capturing an image. The characteristic time for heat diffusion out of alloy films during phase transformation $(\tau'_{\rm film})$ are $7.06\times 10^{-6}\,{\rm s}\,(L=1.45\times 10^{-5}\,{\rm m}),$ $2.54\times 10^{-6}\,{\rm s}\,(L=8.7\times 10^{-6}\,{\rm m}),$ and $2.82\times 10^{-7}\,{\rm s}\,(L=2.9\times 10^{-6}\,{\rm m}),$ when $C_p\approx 420\,{\rm J/(kg\cdot K)},$ $\rho\approx 8\times 10^3\,{\rm kg/m^3},$ $\kappa\approx 100\,{\rm W/(m\cdot K)}$ [67]. According to Equation (5), the Fo of the Ni–Mn–Sn alloy film, Fo_{film}, is $8\times 10^6\gg 1$. Thus, time for heat to conduct through Ni–Mn–Sn alloy film is not limiting. Similarly, we consider the effect of thermal diffusion from the temperature stage through the tungsten substrate. The characteristic time of the tungsten substrate for heat to conduct between the temperature stage and alloy films (τ'_w) is $4.00\times 10^{-5}\,{\rm s}\,(L=5.0\times 10^{-5}\,{\rm m}),$ when $C_p\approx 135\,{\rm J/(kg\cdot K)},$ $\rho\approx 1.93\times 10^4\,{\rm kg/m^3},$ $\kappa\approx 163\,{\rm W/(m\cdot K)}.$ The Fo of the tungsten substrate, Fow, is $1\times 10^6\gg 1$. Thus, the time for heat to conduct through the tungsten substrate also is not limiting, and would not contribute significantly to measured hysteresis. Size effects in hysteresis of microscale samples, which have high heat

exchange rates with their environment and do not undergo thermal excursion, are attributable to the enhanced internal frictional work during transformation, associated with an increase in surface area and volume ratio [23].

Generally, internal friction represents a resistance to interface motion due to the existence of internal defects which are associated with energy barriers during phase transformation [68]. Defect induced internal friction includes a diffusive redistribution of point defects under an applied stress and dislocation motion associated with an elongation of dislocation line [68]. Overcoming energy barriers at interphase boundaries and grain boundaries could induce internal friction [69]. As other potential origins of hysteretic effects have been discounted, we conclude that internal friction represents the dominant contribution to hysteresis, and proceed to interpret thickness-dependent hysteresis under this paradigm.

4.2. A model of thickness-dependent hysteresis

Size effects in film hysteresis during phase transformation are strongly correlated with film thickness. Logarithms of area (S) (Fig. 8a), volume (V) (Fig. 8b), and thickness (t) of hundreds of grains with known A_f and M_s temperatures, show linear correlations with corresponding log ΔT_0^{hyst} . However, for grains within a single film (constant thickness), the correlations between grain log ΔT_0^{hyst} and log S or log V are illustrated by r (Table 3), when we assume that all variables are normally distributed based on diagnostic plots of their normal probabilities (Fig. S8). These r < 0.50 and show low correlations [59]. Besides, linear fits of $\log S$ on $\log t$ ($\log S =$ $(1.12 \pm 0.03) - 1.49 \log t$, $R^2 = 0.65$, r = 0.81) (Fig. 8c) or $\log V$ on $\log t$ $(\log V = (1.15 \pm 0.03) - 2.47 \log t, R^2 = 0.84, r = 0.92)$ (Fig. 8d) show that grain area and volume are strongly correlated with grain thickness, which is equal to film thickness. Therefore, apparent correlations between grain area or grain volume and ΔT_0^{hyst} are primarily attributable to film thickness, and the fact that film thickness itself strongly correlates with grain area and volume.

Thickness-dependent hysteresis is quantified by a power law $(\Delta T_0^{hyst} = \mathbf{a} \cdot t^{\mathbf{b}},$ a = 24.73, b = -0.50, $2.9 \,\mu\text{m} \le t \le 14.5 \,\mu\text{m}$) (Fig. 8e). Log t of grains show a linear correlation with corresponding $\log \Delta T_0^{hyst}$. Thus, the power law model is chosen to elucidate scaling relationships that govern size dependent hysteresis in Heusler alloy films. In a previous study, Cu-Al-Ni microwires showed size dependent thermal hysteresis, which was calculated by endothermic peak temperature minus exothermic peak temperature in DSC test [23]. Microwire diameters (D) are transformed to film thickness by an equation t = D/4, because the surface area and volume ratio is 4/D in microwires and 1/t in alloy films, and are plotted with the corresponding thermal hysteresis beside our thickness-dependent hysteresis model (Fig. 8e). The relation between hysteresis and transformed diameters in microwires could also be quantified by a power law model $(\Delta T_0^{hyst} = a' \cdot t^{b'})$, a' = 23.66, b' = -0.25, $R^2 = 0.75$, $39 \, \mu \text{m} \le t \le 117 \, \mu \text{m})$. Thus, power law models are suitable to elucidate size dependent hysteresis in Heusler alloy films with thickness in the range of (2.9 to nearly 100) µm.

3. Size effects based on defects induced internal friction

Thickness-dependent hysteresis, which has been attributed to the internal friction-induced energy dissipation in microscale alloy films, is caused by pinning effects of defects at the film/substrate interface [23]. As we discussed previously, size effects in hysteresis of microscale samples are attributable to the internal frictional work. According to the linear fit of calculated $E_{\rm diss}$ on $\Delta T_0^{\rm hyst}$ in Fig. 4, the internal frictional work ($E_{\rm fr}$) of Ni–Mn–Sn alloy films during phase transformations is quantified by the following power law

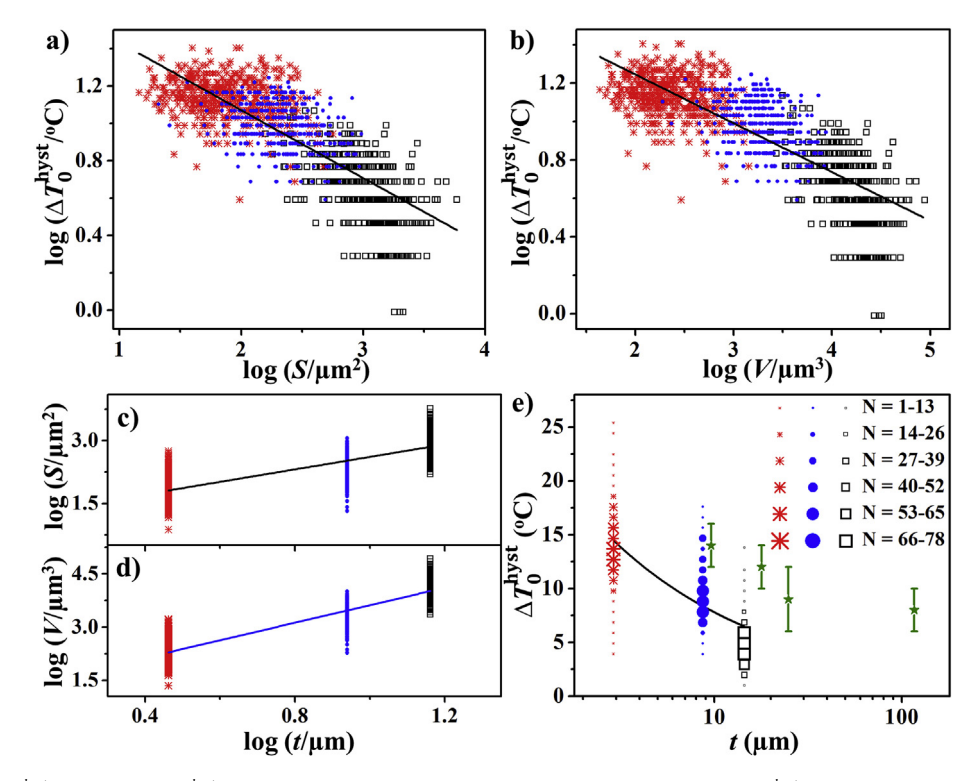


Fig. 8. Linear fits of a) $\log \Delta T_0^{hyst}$ on $\log S$, b) $\log \Delta T_0^{hyst}$ on $\log V$, c) $\log S$ on $\log V$, d) $\log V$ on $\log V$, and the power law fit of e) ΔT_0^{hyst} on film thickness for 14.5 (black square), 8.7 (blue circle), and 2.9 (red asterisk) μ m thick alloy films. Green stars with uncertainty show the hysteresis of Cu–Al–Ni microwires on transformed diameters [23]. (For interpretation of the references to colour in this figure legend, the reader is referred to the Web version of this article.)

Table 3 r between grain $\log \Delta T_0^{hyst}$ and $\log S$ or $\log V$ in each film.

r	$\log \Delta T_0^{hyst}$ and $\log S$ or $\log V$
14.5 μm film	0.45
8.7 μm film	0.37
2.9 μm film	0.20

model (Equation (6)),

$$\begin{split} E_{\rm fr} = & E_{\rm diss} = (2.80 \pm 0.07) \cdot \Delta T_0^{\rm hyst} \approx 2.80 \cdot 24.73 \cdot t^{-0.50} \\ & = 69.24 \cdot t^{-0.50} \; (\rm J/mol). \end{split} \tag{6}$$

We envision that the defects are caused by residual stress, which is generated due to thermal expansion mismatch, and concentrates at the film/substrate interface. The thinner the film is, the smaller the grain size is, and the stronger the pinning effect is at the film/substrate interface. Thus, with the decreasing of film thickness, more energy is dissipated during phase transformations by the enhanced internal frictional work, which increases hysteresis.

5. Conclusions

Thickness-dependent hysteresis in Ni–Mn–Sn Heusler alloy films is demonstrated by analyzing the correlations between thermal hysteresis and grain size or film thickness. Microscale Ni_{0·48}Mn_{0·40}Sn_{0.12} alloy films with decreasing thickness were synthesized by post-annealed multi-layer films using electrochemical deposition in multi-pot aqueous solutions. By observing phase transformation behavior of nearly four hundred grains on each film, the thermal hysteresis and size of the grains were obtained. By analyzing the correlations between hysteresis and grain area or volume within a single film, it was found that hysteresis was

not correlated with grain size, but it increased with decreasing film thickness following a power law relationship. After eliminating the negligible or recoverable effects, thickness-dependent hysteresis in microscale samples was attributed to the internal friction-induced energy dissipation at the film/substrate interface.

Declarations of interest

The authors declare no competing interests.

Data availability statement

The datasets generated and analyzed during the current study are available from the corresponding author on reasonable request. All data generated or analyzed during this study are included in this published article and its supplementary information file.

Acknowledgements

The authors acknowledge support from National Science Foundation under Grant No. 1636105. The authors wish to thank Dr. Zhengyang Zhou for reviewing the statistical analysis presented in this work.

Appendix A. Supplementary data

Supplementary data to this article can be found online at https://doi.org/10.1016/j.actamat.2019.09.001.

References

- J.M. Jani, M. Leary, A. Subic, M.A. Gibson, A review of shape memory alloy research, applications and opportunities, Mater. Des. 56 (2014) 1078–1113.
- [2] T. Tadaki, K. Otsuka, K. Shimizu, Shape memory alloys, Annu. Rev. Mater. Sci.

- 18 (1988) 25-45.
- [3] A. Planes, E. Stern-Taulats, T. Castan, E. Vives, L. Mañosa, A. Saxena, Caloric and multicaloric effects in shape memory alloys, Mater. Today: SAVE Proc. 2 (2015) S477—S484.
- [4] S. Fähler, V.K. Pecharsky, Caloric effects in ferroic materials, MRS Bull. 43 (2018) 264–268.
- [5] S. Fähler, U.K. Rößler, O. Kastner, J. Eckert, G. Eggeler, H. Emmerich, P. Entel, S. Müller, E. Quandt, K. Albe, Caloric effects in ferroic materials: new concepts for cooling. Adv. Eng. Mater. 14 (2012) 10–19.
- [6] R. Zarnetta, R. Takahashi, M.L. Young, A. Savan, Y. Furuya, S. Thienhaus, B. Maaß, M. Rahim, J. Frenzel, H. Brunken, Identification of quaternary shape memory alloys with near-zero thermal hysteresis and unprecedented functional stability, Adv. Funct. Mater. 20 (2010) 1917–1923.
- [7] A. Diestel, P. Chekhonin, R. Niemann, W. Skrotzki, K. Nielsch, S. Fähler, Reducing thermal hysteresis in epitaxial Ni–Mn–Ga–Co films by transformation cycling. Phys. Status Solidi B 255 (2018) 1700330.
- [8] A. Diestel, R. Niemann, B. Schleicher, K. Nielsch, S. Fähler, Reducing hysteresis losses by heating minor loops in magnetocaloric Ni–Mn–Ga–Co films, Energy Technol. 6 (2018) 1463–1469
- [9] P.J.S. Buenconsejo, R. Zarnetta, M. Young, H. Brunken, A. Mehta, A. Ludwig, On the mechanism that leads to vanishing thermal hysteresis of the B2-R phase transformation in multilayered (TiNi)/(W) shape memory alloy thin films, Thin Solid Films 564 (2014) 79–85.
- [10] H. Sepehri-Amin, A. Taubel, T. Ohkubo, K. Skokov, O. Gutfleisch, K. Hono, Microstructural origin of hysteresis in Ni-Mn-In based magnetocaloric compounds, Acta Mater. 147 (2018) 342–349.
- [11] J. Cui, Y.S. Chu, O.O. Famodu, Y. Furuya, J. Hattrick-Simpers, R.D. James, A. Ludwig, S. Thienhaus, M. Wuttig, Z. Zhang, Combinatorial search of thermoelastic shape-memory alloys with extremely small hysteresis width, Nat. Mater. 5 (2006) 286.
- [12] D. Zhao, J. Liu, X. Chen, W. Sun, Y. Li, M. Zhang, Y. Shao, H. Zhang, A. Yan, Giant caloric effect of low-hysteresis metamagnetic shape memory alloys with exceptional cyclic functionality, Acta Mater. 133 (2017) 217–223.
- [13] E. Lovell, A.M. Pereira, A.D. Caplin, J. Lyubina, L.F. Cohen, Dynamics of the first-order metamagnetic transition in magnetocaloric La(Fe,Si)₁₃: reducing hysteresis, Adv. Energy Mater. 5 (2015) 1401639.
- [14] N. Teichert, A. Auge, E. Yüzüak, I. Dincer, Y. Elerman, B. Krumme, H. Wende, O. Yildirim, K. Potzger, A. Hütten, Influence of film thickness and composition on the martensitic transformation in epitaxial Ni–Mn–Sn thin films, Acta Mater. 86 (2015) 279–285.
- [15] N. Teichert, D. Kucza, O. Yildirim, E. Yuzuak, I. Dincer, A. Behler, B. Weise, L. Helmich, A. Boehnke, S. Klimova, Structure and giant inverse magnetocaloric effect of epitaxial Ni-Co-Mn-Al films, Phys. Rev. B 91 (2015) 184405.
- [16] V.M. Andrade, R.C. Vivas, S.S. Pedro, J.C.G. Tedesco, A.L. Rossi, A.A. Coelho, D.L. Rocco, M.S. Reis, Magnetic and magnetocaloric properties of La_{0.6}Ca_{0.4}MnO₃ tunable by particle size and dimensionality, Acta Mater. 102 (2016) 49–55.
- [17] J. San Juan, M.L. Nó, C.A. Schuh, Nanoscale shape-memory alloys for ultrahigh mechanical damping, Nat. Nanotechnol. 4 (2009) 415.
- [18] H. Ossmer, C. Chluba, M. Gueltig, E. Quandt, M. Kohl, Local evolution of the elastocaloric effect in TiNi-based films, Shape Mem. Superelasticity 1 (2015) 142–152.
- [19] C.-W. Nan, L. Liu, N. Cai, J. Zhai, Y. Ye, Y. Lin, L. Dong, C. Xiong, A three-phase magnetoelectric composite of piezoelectric ceramics, rare-earth iron alloys, and polymer, Appl. Phys. Lett. 81 (2002) 3831–3833.
- [20] D.T. Queheillalt, Y. Katsumura, H.N. Wadley, Synthesis of stochastic open cell Ni-based foams, Scr. Metall. 50 (2004) 313–317.
- [21] P.J.S. Buenconsejo, R. Zarnetta, A. Ludwig, The effects of grain size on the phase transformation properties of annealed (Ti/Ni/W) shape memory alloy multilayers, Scr. Metall. 64 (2011) 1047–1050.
- [22] J. Ortin, A. Planes, Thermodynamic analysis of thermal measurements in thermoelastic martensitic transformations, Acta Metall. 36 (1988) 1873–1889.
- [23] Y. Chen, C.A. Schuh, Size effects in shape memory alloy microwires, Acta Mater. 59 (2011) 537–553.
- [24] R. Cech, D. Turnbull, Heterogeneous nucleation of the martensite transformation, J. Metals 8 (1956) 124–132.
- [25] G. Olson, K. Tsuzaki, M. Cohen, Statistical aspects of martensitic nucleation, Mater. Res. Soc. Symp. Proc. 57 (1985).
- [26] I.-W. Chen, Y. Chiao, K. Tsuzaki, Statistics of martensitic nucleation, Acta Metall. 33 (1985) 1847–1859.
- [27] M. Umemoto, W. Owen, Effects of austenitizing temperature and austenite grain size on the formation of athermal martensite in an iron-nickel and an iron-nickel-carbon alloy, Metall. Trans. 5 (1974) 2041–2046.
- [28] P. Brofman, G. Ansell, On the effect of fine grain size on the M s temperature in Fe-27Ni-0.025 C alloys, Metall. Trans. A 14 (1983) 1929–1931.
- [29] C. Hayzelden, B. Cantor, The martensite transformation in Fe-Ni-C alloys, Acta Metall. 34 (1986) 233—242.
- [30] K. Seki, H. Kura, T. Sato, T. Taniyama, Size dependence of martensite transformation temperature in ferromagnetic shape memory alloy FePd, J. Appl. Phys. 103 (2008), 063910.
- [31] D.N. Adnyana, Effect of grain size on transformation temperatures in a grain-refined, copper-based, shape-memory alloy, Metallography 19 (1986) 187–196.
- [32] K. Mukunthan, L. Brown, Preparation and properties of fine grain β -CuAlNi

- strain-memory alloys, Metall. Trans. A 19 (1988) 2921-2929.
- [33] C.L. del Castillo, B. Mellor, M. Blazquez, C. Gomez, The influence of composition and grain size on the martensitic transformation temperatures of Cu-Al-Mn shape memory alloys, Scr. Metall. 21 (1987) 1711–1716.
- [34] S. Montecinos, A. Cuniberti, A. Sepúlveda, Grain size and pseudoelastic behaviour of a Cu–Al–Be alloy, Mater. Char. 59 (2008) 117–123.
- [35] Y. Sutou, T. Omori, K. Yamauchi, N. Ono, R. Kainuma, K. Ishida, Effect of grain size and texture on pseudoelasticity in Cu–Al–Mn-based shape memory wire, Acta Mater. 53 (2005) 4121–4133.
- [36] G. Sure, L. Brown, The mechanical properties of grain refined β-cuaini strainmemory alloys, Metall. Mater. Trans. A 15 (1984) 1613–1621.
- [37] M. Somerday, J. Wert, R. Comstock, Effect of grain size on the observed pseudoelastic behavior of a Cu-Zn-Al shape memory alloy, Metall. Mater. Trans. A 28 (1997) 2335—2341.
- [38] I. Dvorak, E. Hawbolt, Transformational elasticity in a polycrystalline Cu-Zn-Sn alloy, Metall. Trans. A 6 (1975) 95–99.
- [39] R. Araya, M. Marivil, C. Mir, O. Moroni, A. Sepúlveda, Temperature and grain size effects on the behavior of CuAlBe SMA wires under cyclic loading, Mater. Sci. Eng. A 496 (2008) 209–213.
- [40] T. Waitz, V. Kazykhanov, H. Karnthaler, Martensitic phase transformations in nanocrystalline NiTi studied by TEM, Acta Mater. 52 (2004) 137–147.
- [41] T. Waitz, T. Antretter, F. Fischer, N. Simha, H. Karnthaler, Size effects on the martensitic phase transformation of NiTi nanograins, J. Mech. Phys. Solids 55 (2007) 419–444.
- [42] T. Waitz, The self-accommodated morphology of martensite in nanocrystalline NiTi shape memory alloys, Acta Mater. 53 (2005) 2273–2283.
- [43] T. Suzuki, M. Shimono, M. Wuttig, Martensitic transformation in micrometer crystals compared with that in nanocrystals, Scr. Metall. 8 (2001) 1979–1982.
- [44] D. König, P. Buenconsejo, D. Grochla, S. Hamann, J. Pfetzing-Micklich, A. Ludwig, Thickness-dependence of the B2–B19 martensitic transformation in nanoscale shape memory alloy thin films: zero-hysteresis in 75 nm thick Ti₅₁Ni₃₈Cu₁₁ thin films, Acta Mater. 60 (2012) 306–313.
- [45] P. Ranzieri, S. Fabbrici, L. Nasi, L. Righi, F. Casoli, V.A. Chernenko, E. Villa, F. Albertini, Epitaxial Ni–Mn–Ga/MgO (1 0 0) thin films ranging in thickness from 10 to 100 nm, Acta Mater. 61 (2013) 263–272.
- [46] R. Vishnoi, R. Singhal, D. Kaur, Thickness dependent phase transformation of magnetron-sputtered Ni–Mn–Sn ferromagnetic shape memory alloy thin films, J. Nano Res. 13 (2011) 3975–3990.
- [47] N. Ozdemir, I. Karaman, N. Mara, Y.I. Chumlyakov, H. Karaca, Size effects in the superelastic response of Ni₅₄Fe₁₉Ga₂₇ shape memory alloy pillars with a two stage martensitic transformation, Acta Mater. 60 (2012) 5670–5685.
- [48] C. Frick, S. Orso, E. Arzt, Loss of pseudoelasticity in nickel—titanium submicron compression pillars, Acta Mater. 55 (2007) 3845—3855.
- [49] D. Norfleet, P. Sarosi, S. Manchiraju, M.-X. Wagner, M. Uchic, P. Anderson, M. Mills, Transformation-induced plasticity during pseudoelastic deformation in Ni–Ti microcrystals, Acta Mater. 57 (2009) 3549–3561.
- [50] A. Ishida, M. Sato, Thickness effect on shape memory behavior of Ti-50.0 at.% Ni thin film, Acta Mater. 51 (2003) 5571–5578.
- [51] Y.Q. Fu, S. Zhang, M. Wu, W.M. Huang, H. Du, J. Luo, A. Flewitt, W. Milne, On the lower thickness boundary of sputtered TiNi films for shape memory application, Thin Solid Films 515 (2006) 80–86.
- [52] U. Gaitzsch, J. Drache, K. McDonald, P. Müllner, P. Lindquist, Obtaining of Ni-Mn-Ga magnetic shape memory alloy by annealing electrochemically deposited Ga/Mn/Ni layers, Thin Solid Films 522 (2012) 171–174.
- [53] S. Franssila, Introduction to Microfabrication, second ed., John Wiley & Sons Ltd, Chichester, 2010.
- [54] Y. Zhang, P.J. Shamberger, Thick film $Ni_{0.5}Mn_{0.5-x}Sn_x$ heusler alloys by multi-layer electrochemical deposition, Sci. Rep. 8 (2018) 11931.
- [55] T. Krenke, M. Acet, E.F. Wassermann, X. Moya, L. Mañosa, A. Planes, Martensitic transitions and the nature of ferromagnetism in the austenitic and martensitic states of Ni–Mn–Sn alloys, Phys. Rev. B 72 (2005), 014412.
- [56] H. Zheng, W. Wang, S. Xue, Q. Zhai, J. Frenzel, Z. Luo, Composition-dependent crystal structure and martensitic transformation in Heusler Ni–Mn–Sn alloys, Acta Mater. 61 (2013) 4648–4656.
- [57] A. Cherechukin, I. Dikshtein, D. Ermakov, A. Glebov, V. Koledov, D. Kosolapov, V. Shavrov, A. Tulaikova, E. Krasnoperov, T. Takagi, Shape memory effect due to magnetic field-induced thermoelastic martensitic transformation in polycrystalline Ni–Mn–Fe–Ga alloy, Phys. Lett. A 291 (2001) 175–183.
- [58] X. Moya, L. Mañosa, A. Planes, T. Krenke, M. Acet, E.F. Wassermann, Martensitic transition and magnetic properties in Ni–Mn–X alloys, Mater. Sci. Eng. A 438 (2006) 911–915.
- [59] M.M. Mukaka, A guide to appropriate use of correlation coefficient in medical research, Malawi Med. J. 24 (2012) 69–71.
- [60] S. Stupkiewicz, H. Petryk, On Dissipation, Interfacial Energy and Size Effects in Shape Memory Alloys, European Symposium on Martensitic Transformations, EDP Sciences, 2009, 03013.
- [61] S. Stupkiewicz, G. Maciejewski, H. Petryk, Low-energy morphology of the interface layer between austenite and twinned martensite, Acta Mater. 55 (2007) 6292–6306.
- [62] E. Bonnot, E. Vives, L. Mañosa, A. Planes, R. Romero, Acoustic emission and energy dissipation during front propagation in a stress-driven martensitic transition, Phys. Rev. B 78 (2008), 094104.
- [63] J. Baram, M. Rosen, On the nature of the thermoelastic martensitic phase transformation in Au-47.5 at.% Cd determined by acoustic emission, Acta Metall. 30 (1982) 655–662.

- [64] X. Wang, Y. Jia, Q. Yao, F. Wang, J. Ma, X. Hu, The calculation of the surface energy of high-index surfaces in metals at zero temperature, Surf. Sci. 551 (2004) 179–188.
- [65] L. Mañosa, A. Planes, D. Rouby, J. Macqueron, Acoustic emission in martensitic transformations, Acta Metall. Mater. 38 (1990) 1635–1642.
 [66] E. Vives, J. Ortín, L. Mañosa, I. Ràfols, R. Pérez-Magrané, A. Planes, Distributions
- of avalanches in martensitic transformations, Phys. Rev. Lett. 72 (1994) 1694.
- [67] V. Sharma, M. Chattopadhyay, R. Kumar, T. Ganguli, P. Tiwari, S. Roy, Magnetocaloric effect in Heusler alloys Ni₅₀Mn₃₄In₁₆ and Ni₅₀Mn₃₄Sn₁₆, J. Phys. Condens. Matter 19 (2007) 496207.

 [68] M.S. Blanter, I.S. Golovin, H. Neuhäuser, H. Sinning, Handbook on Internal
- Friction in Metallic Materials, Springer, Berlin, 2007.
- [69] A. Roitburd, Martensitic transformation as a typical phase transformation in solids, Solid State Phys. 33 (1978) 317-390.